



This is a repository copy of *Surveying the effects of aging a high C-containing co-based superalloy from the As-cast and solution heat-treated conditions.*

White Rose Research Online URL for this paper:

<https://eprints.whiterose.ac.uk/209348/>

Version: Published Version

---

**Article:**

Moffat, J.P., Christofidou, K.A., Pek, M.E. et al. (3 more authors) (2024) Surveying the effects of aging a high C-containing co-based superalloy from the As-cast and solution heat-treated conditions. *Metallurgical and Materials Transactions A*, 55 (3). pp. 791-802. ISSN 1073-5623

<https://doi.org/10.1007/s11661-023-07283-7>

---

**Reuse**

This article is distributed under the terms of the Creative Commons Attribution (CC BY) licence. This licence allows you to distribute, remix, tweak, and build upon the work, even commercially, as long as you credit the authors for the original work. More information and the full terms of the licence here:

<https://creativecommons.org/licenses/>

**Takedown**

If you consider content in White Rose Research Online to be in breach of UK law, please notify us by emailing [eprints@whiterose.ac.uk](mailto:eprints@whiterose.ac.uk) including the URL of the record and the reason for the withdrawal request.



[eprints@whiterose.ac.uk](mailto:eprints@whiterose.ac.uk)  
<https://eprints.whiterose.ac.uk/>

# Surveying the Effects of Aging a High C-Containing Co-Based Superalloy From the As-Cast and Solution Heat-Treated Conditions



JAMES P. MOFFAT, KATERINA A. CHRISTOFIDOU, MING EN PEK,  
NICHOLAS G. JONES, PAUL JACKSON, and HOWARD J. STONE

The microstructure of the high carbon-containing cobalt-based superalloy, Co-101, has been studied in the as-cast state and following a variety of heat treatments. In the as-cast state both  $M_7C_3$  and Mo-rich  $M_{23}C_6$  carbides were observed in the interdendritic regions. After thermal exposure at temperatures between 1000 °C and 1250 °C for 1, 10, and 100 hours, the  $M_7C_3$  interdendritic carbide network was observed to transform into a Mo-lean  $M_{23}C_6$  carbide. These changes were rationalized with thermodynamic calculations. The carbide transformation liberated carbide-forming elements that resulted in the precipitation of intragranular carbides in the dendritic regions at temperatures below 1150 °C. These carbides in the cast-aged material preferentially formed at the dendrite peripheries early during exposure, leading to wide particle size distributions. Peak hardness in the cast-aged material was attained within the first 10 hours of exposure and softening was observed thereafter. After solution heat treating at 1250 °C for 10 hours, the microstructure of Co-101 comprised an  $M_{23}C_6$  interdendritic carbide network and solid solution dendrites supersaturated with carbide-forming elements. Subsequent aging of this microstructure for 100 hours at 900 °C led to a high number density and narrow particle size distribution of intragranular carbides. The characteristics of these carbides in the solution-aged material resulted in greater hardness, which was retained for longer durations of exposure, than the cast-aged specimens.

<https://doi.org/10.1007/s11661-023-07283-7>  
© The Author(s) 2024

## I. INTRODUCTION

COBALT-BASED superalloys are ubiquitous in applications that require high oxidation/corrosion resistance and good mechanical properties at service temperatures ranging from 700 °C to 1200 °C including aerospace engine components,<sup>[1]</sup> wear-resistant bearings, and hard-facing surfaces.<sup>[2]</sup> Many Co-based superalloys achieve their high-temperature strength and creep resistance through a solid-solution hardened Co-rich matrix ( $\gamma$ ) reinforced inter- and intra-granularly by a dispersion of hard carbide phases.<sup>[3,4]</sup> Importantly, the mechanical properties of the alloy are influenced by several factors, including composition, phase fractions, carbide

morphology, and precipitate dispersity,<sup>[5,6]</sup> all of which depend on the service temperature and duration of exposure. As such, it is critical that the evolution of the carbide phases during prolonged exposure at elevated temperatures is understood so that long-duration stability of the mechanical properties are attained. For example, studies of the nozzle guide vane Co-alloys FSX-414 by Luna Ramirez *et al.*<sup>[7]</sup> and X-45 by Zangeneh *et al.*,<sup>[8,9]</sup> have shown that the nature of carbide precipitation significantly impacts the mechanical properties in the service environment. The volume fraction of the carbide phases in FSX-414 was observed to increase between 560 °C and 934 °C and, similarly for X-45 between 816 °C and 927 °C. In both cases, this occurred due to extensive precipitation of the  $M_{23}C_6$  carbides.<sup>[8]</sup> The precipitation of needle-like carbides was also observed within the interior of the grains on stacking faults in both alloys, which was found to accelerate fracture initiation and propagation, particularly around grain boundaries and interdendritic carbides after long exposure times.<sup>[9]</sup>

Modification of the carbide distribution may be readily achieved in Co-based superalloys through high-temperature heat treatment. Specifically, multi-step anneal-age heat treatments have been shown to be

JAMES P. MOFFAT, MING EN PEK, NICHOLAS G. JONES, and HOWARD J. STONE are with the Department of Materials Science and Metallurgy, University of Cambridge, 27 Charles Babbage Road, Cambridge, CB3 0FS, UK. Contact e-mail: [hjs1002@cam.ac.uk](mailto:hjs1002@cam.ac.uk)  
KATERINA A. CHRISTOFIDOU is with the Department of Materials Science and Engineering, The University of Sheffield, Sir Robert Hadfield Building, Mappin Street, Sheffield, S1 3JD, UK.  
PAUL JACKSON is with the Knauf Insulation Ltd., PO Box 10, Stafford Road, St Helens, Merseyside, WA10 3NS, UK.

Manuscript submitted April 20, 2023; accepted December 7, 2023.

Article published online January 31, 2024

advantageous in low C-containing Co-based alloys, including DZ40M,<sup>[10]</sup> wrought Haynes 25, and S-816.<sup>[11]</sup> In alloys of this type complete solutioning of the primary carbides is possible. This allows the possibility of dissolution of blocky or interdendritic carbides produced in the as-cast state, which may be precipitated as a fine dispersion of intragranular and intergranular carbides during subsequent aging. Such microstructural modification may be exploited to achieve more desirable mechanical properties for a specific application. In contrast, the primary interdendritic carbides in high C-containing alloys cannot be fully redistributed through annealing. For example, a study of the high C-containing Co-based alloy Co-101 identified  $M_7C_3$  and  $M_{23}C_6$  carbides in the as-cast state, which persisted within the interdendritic regions of the alloy microstructure at all temperatures below the solidus.<sup>[12]</sup> This limited the ability to solution carbides during subsequent heat treatment, restricting the processing of such alloys to single-step heat treatments or service use in the as-cast state. However, studies have identified the potential merits of annealing and aging heat treatments to form preferred carbide types and stabilized matrix carbide interfaces.<sup>[13]</sup> Such heat treatments have also been shown to transform the carbides. For example, the primary chromium carbides have been seen to transform from  $M_7C_3$  to  $M_{23}C_6$  during prolonged exposures at 1000 °C for an austenitic stainless steel<sup>[14]</sup> and at 500 °C to 600 °C in a ferritic stainless steel.<sup>[15]</sup> It is clear that such behavior is sensitive to specific alloy composition and further studies are therefore warranted.

In this study, the microstructural changes that occur following exposure at a wide range of temperatures in the high C-containing Co-based superalloy Co-101 have been studied along with the associated hardness. The conditions considered span the temperature range over which carbide coarsening and dissolution may be expected to occur during exposure for up to 100 hours.

## II. MATERIALS AND METHODS

The investigated alloy, Co-101, with the nominal composition quoted in Table I, was produced by investment casting. Specimens for heat treatment were prepared by sealing approximately  $10 \times 10 \times 7$  mm as-cast material in argon back-filled quartz ampoules. To assess the effect of single-step heat treatments, specimens were exposed for 1, 10, and 100 hours at temperatures of 900 °C, 950 °C, 1000 °C, 1050 °C, 1100 °C, 1150 °C, 1200 °C, and 1250 °C. To assess the effect of two-step heat treatments, three conditions were considered. For each condition, the first step was solution heat treatment at 1250 °C for 10 hours. These conditions were selected as they enabled dissolution of some of the interdendritic carbides while avoiding intragranular precipitation during the solution heat treatment. This solution heat treatment was followed by a 100-hour aging treatment at 900 °C, 1000 °C, or 1100 °C to promote controlled intragranular precipitation. All specimens were inserted into the furnace at the set point temperatures and quenched into iced water on

removal from the furnace. Specimens subjected to two heat treatment steps were quenched into iced water between the solutioning and aging steps.

Microstructural characterization of the specimens was performed using scanning electron microscopy (SEM), imaging in the backscattered electron (BSE) mode at a 20 kV accelerating voltage in a Carl Zeiss GeminiSEM 300 instrument. Elemental analysis of the alloy and its constituent phases was performed using energy-dispersive X-ray spectroscopy (EDX) during SEM using an Oxford Instruments 50 mm<sup>2</sup> X-max<sup>n</sup> detector. The carbon signal was omitted from measurements due to the ubiquitous carbon-based contamination on the specimen surface. Prior to microstructural examination, the specimen surfaces were prepared using conventional metallographic techniques, using sequentially finer grades of SiC grinding papers, diamond polishing solutions, and finally, a 0.04 μm colloidal silica polishing suspension.

Image analysis to quantify microstructural features was performed using the ImageJ software package.<sup>[16]</sup> Phase fraction analyses were performed over single images of regions with a minimum area of 0.89 mm<sup>2</sup>, while carbide particle size distributions were obtained from single images at higher magnification over regions with a minimum area of 0.039 mm<sup>2</sup>. To ensure accurate phase fraction determination, bandpass filters were applied to assist with the contrast thresholding. Contour plots of the phase fractions were produced using the Wavemetrics Igor Pro software package applying a linear interpolation between the data points for each heat treatment. Due to the similarity between the contrasts of the precipitates and dark contrast interdendritic phase, the interdendritic regions were manually masked from the micrographs prior to the particle size distribution (PSD) analysis. For the particle size analysis, precipitates were defined as clusters of adjacent pixels greater than 1, a Ferret diameter less than 16 μm, and a spheroidicity between 0 and 1, ensuring to omit particles touching the edges of the micrograph.

The hardness of the specimens was determined following ASTM E92-17. Data were collected using a 5 kgf pyramidal Vickers indenter fitted to a 200HV-5 instrument. The calibration of the instrument was assessed with a standard steel test block before collecting data from at least 8 indents from each specimen to achieve statistically relevant results. Before testing, the specimen surfaces were ground and polished with a protocol culminating in a 1 μm diamond polish.

Phase identification in the alloys was performed with X-ray diffraction (XRD) using a Bruker D8 ADVANCE Davinci instrument fitted with a LynxEye EX position sensitive detector. For these measurements, samples approximately  $10 \times 10$  mm were polished to a 1 μm diamond finish. Diffraction data were collected from the samples with Ni-filtered Cu K $\alpha$  radiation between 30 and 90 deg  $2\theta$ . The specimens were rotated at 30 revolutions per minute during data acquisition to improve grain sampling. Peak fitting was performed using a full pattern Pawley refinement in the TOPAS-Academic software package.

**Table I. Nominal and EDX-Determined Compositions of the Co-101 Alloy.**

Alloy		Composition							
		Co	Cr	Ni	Mo	Fe	Si	Mn	C
Nominal	Wt Pct	bal.	30.0	10.0	5.0	3.0	0.6	0.5	0.5
	At. Pct	bal.	32.4	9.6	2.9	3.0	1.2	0.5	2.3
EDX	Wt Pct	bal.	33.9	9.9	4.9	1.2	0.7	0.6	—
	At. Pct	bal.	37.1	9.6	2.9	1.2	1.5	0.7	—

High-temperature phase transformations within the heat-treated alloys were determined using differential scanning calorimetry (DSC) with a Netzsch 404 instrument. For these measurements, electro-discharge machining (EDM) was used to produce approximately 5 mm diameter and 1.2 mm tall specimens. For all samples, the EDM recast layer was removed prior to testing by manual grinding with SiC paper. The specimens were loaded into loose-lidded alumina crucibles and DSC data acquired under a 50 mL/min flowing argon atmosphere. All specimens were heated from 50 °C to 1450 °C at a rate of 10 °C/min.

Simulations of the phase fractions and phase compositions expected in Co-101 as a function of temperature were performed using the Thermo-Calc 2022b software with the SSOL5 database. Calculations were performed assuming equilibrium and Scheil solidification conditions.

### III. RESULTS

#### A. The Microstructure of As-Cast and Heat-Treated Co-101

The microstructure of as-cast Co-101 was observed to have a continuous matrix phase with a skeletal interdendritic network consisting of two phases, one bright and one dark in BSE contrast, as shown in Figure 1(a). Previous microstructural characterization of the as-cast Co-101 identified the bright contrast phase to be Mo-rich  $M_{23}C_6$  and the dark contrast phase to be  $M_7C_3$ .<sup>[12]</sup> The high magnification insets of Figure 1(a) show the interlamellar morphology of the bright contrast  $M_{23}C_6$  phase, and the so-called ‘fishbone’ morphology of the dark contrast  $M_7C_3$  phase. The 900 °C, 1000 °C, and 1100 °C 100-hour aged microstructures of Co-101 are shown in Figures 1(b) through (d), respectively. The heat-treated conditions exhibited variations in the microstructural features compared to the as-cast state. The bright contrast  $M_{23}C_6$  phase lost the fine interlamellar morphology following heat treatment above 900 °C and reduced in areal fraction with increasing temperature. The dark contrast phase showed increasing spheroidization at higher temperatures, exchanging the ‘fishbone’ morphology for a blocky or globular morphology. Importantly, it should be noted that the dark contrast interdendritic phase, when exposed to temperatures above 1000 °C, exhibited variations in contrast, as can be observed towards the

bottom right-hand corner of the high magnification inset of Figure 1(c). The insets of Figure 1(b) through (d) highlight the dark contrast precipitates that formed in the matrix during high-temperature exposure. These precipitates possessed a similar contrast to the dark BSE interdendritic phase, with a cuboidal shape, and were more abundant at the dendrite peripheries in all heat-treated specimens. In the 1000 °C aged specimen, the number of precipitates appeared to have increased compared to the 900 °C specimen, whereas, in the 1100 °C specimen, the precipitates showed evidence of agglomeration and a reduction in number density. In the 1000 °C specimen, precipitation was observed deeper into the matrix dendrites compared to the 900 °C and 1100 °C specimens. It should be noted that the interdendritic carbides and the matrix containing precipitates were separated by a precipitation-free zone.

The temporal evolution of the phase distributions in Co-101 following exposure at high temperatures are shown as contour plots in Figure 2. The matrix, the dark BSE-contrast interdendritic and precipitation phases, and the bright BSE-contrast phase are shown in Figures 2(a) through (c), respectively. As shown in Figure 2(a), for the majority of temperatures, the matrix phase fraction was lowest after 10 hours and increased with further exposure. In Figure 2(b), the dark BSE-contrast interdendritic and precipitation phases demonstrated inverse behavior to the matrix (Figure 2(a)), with a maximum phase fraction after 10 hours of exposure at most temperatures. This increase in the fraction of the dark BSE-contrast phase suggests the formation of precipitates after 10 hours. In Figure 2(c), the bright BSE-contrast phase fraction was observed to decrease following exposure at all temperatures for times between 1 and 10 hours. Above 1100 °C for all exposure times, the bright BSE-contrast phase was not detected in the micrographs. However, at temperatures between 900 °C and 1050 °C, after the phase fraction decreased significantly between 1 and 10 hours, the bright BSE-contrast phase was observed to increase again after 100 hours of exposure.

Figure 3(a) shows the microstructures of Co-101 following a 1250 °C 10-hour solution heat treatment (SHT), and the specimens subjected to the SHT and an additional age (SHT-A) at 900 °C, 1000 °C, and 1100 °C for 100 hours, Figures 3(b) through (d), respectively. In Figure 3(a), the microstructure of Co-101 in the SHT state comprises two major phases, the continuous matrix, and a dark BSE-contrast interdendritic phase.



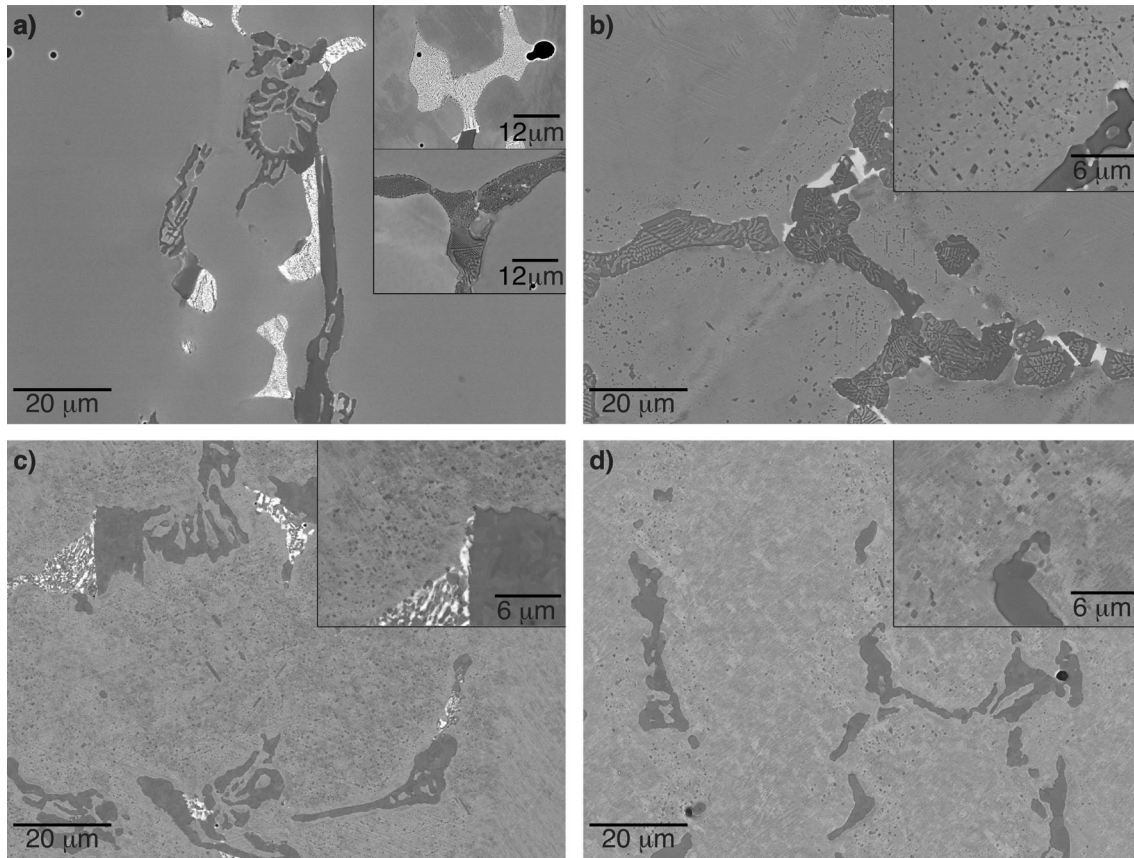


Fig. 1—BSE SEM micrographs of as-cast Co-101 (a), and after aging for 100 h at 900 °C (b), 1000 °C (c), and 1100 °C (d).

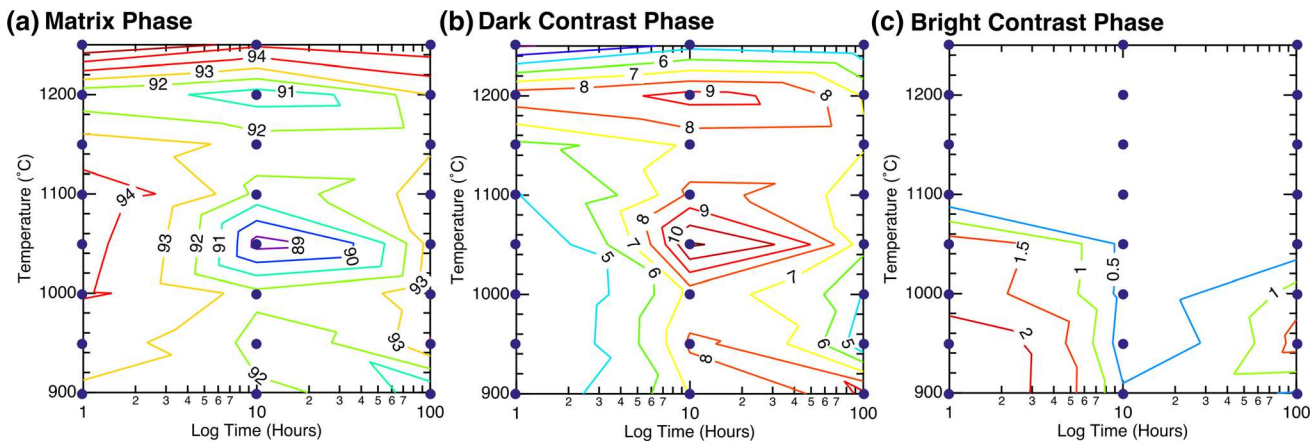


Fig. 2—Contour plots showing the areal phase fractions of the matrix (a), the dark contrast BSE phase (b), and the bright contrast BSE phase (c), present in Co-101 after heat-treating from the as-cast state. The individual heat treatment conditions used to construct the contour plots are represented by the blue circles (Color figure online).

The interdendritic phase showed evidence of spheroidization with a reduction in continuity between the carbide islands compared with the as-cast state, Figure 1. The bright BSE-contrast Mo-rich M<sub>23</sub>C<sub>6</sub> phase observed in the as-cast material, Figure 1(a) was not present in the microstructure, suggesting it had been dissolved during the SHT. Figure 3(b) shows the microstructure of Co-101 after an SHT-A at 900 °C, which contained a similarly spheroidized interdendritic

network to the SHT specimen. However, the additional aging induced the formation of a bright BSE-contrast phase, stochastically decorating the interdendritic and matrix phase interfaces. Furthermore, as highlighted by the inset, secondary precipitation of a dark BSE-contrast phase was also observed within the matrix.

Figure 3(c) shows the microstructure of the SHT-A 1000 °C specimen, which exhibited similar features to the SHT-A 900 °C specimen. The interdendritic network

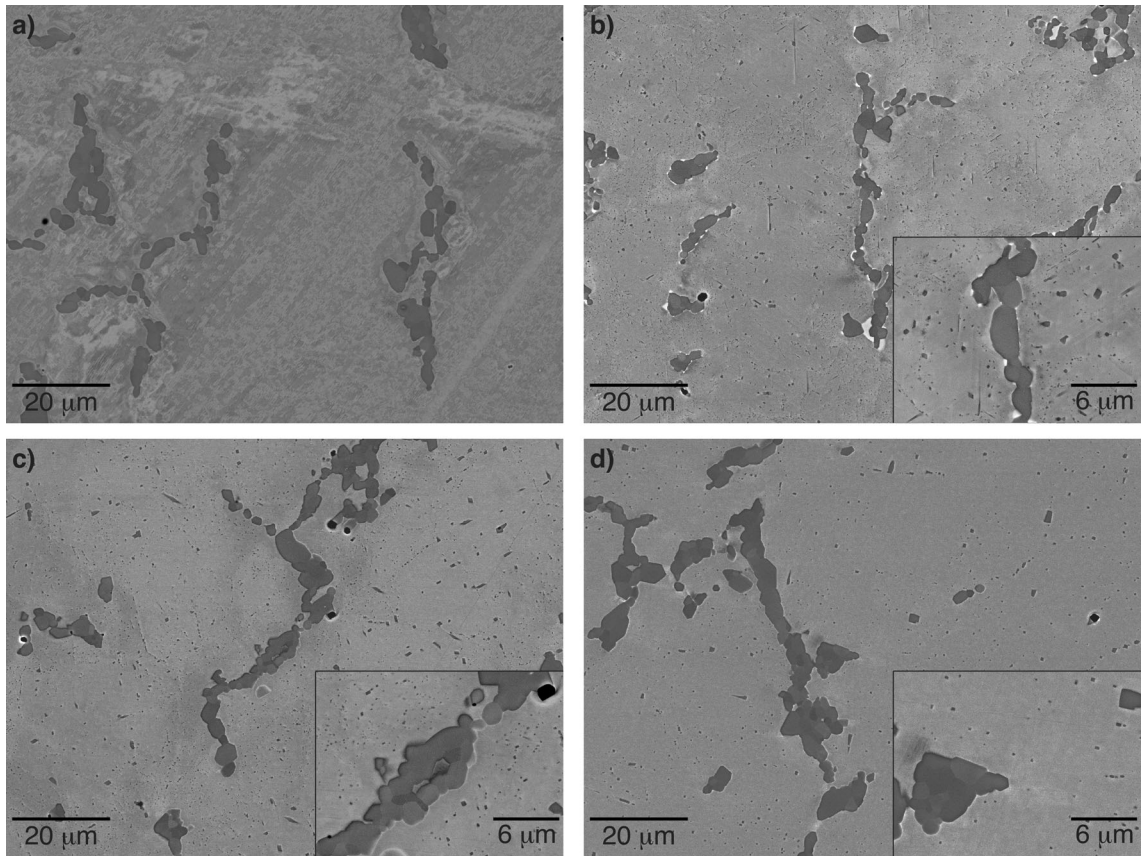


Fig. 3—BSE SEM micrographs of Co-101 following a solution heat treatment of 10 h at 1250 °C (a) and after post-solution aging for 100 h at 900 °C (b), 1000 °C (c), and 1100 °C (d).

shows evidence of spheroidization, but the bright BSE-contrast phase was not as discernible. The precipitates formed in the matrix phase also appeared to be coarser compared to the SHT-A 900 °C specimen. The microstructure of the SHT-A 1100 °C specimen, in Figure 3(d), was similar to the other SHT and SHT-A specimens. However, significant coarsening of the precipitates could be observed and fewer were present in the microstructure.

Figure 4 shows the phase fractions between the as-cast and additional 900 °C, 1000 °C, and 1100 °C 100-hour aged specimens (solid bars) and the SHT and SHT-A specimens (striped bars). The blue, green, and purple bars represent the matrix, dark BSE-contrast, and bright BSE-contrast phases, respectively. The application of the SHT has a pronounced effect upon the phase constituents. Prior to aging, a greater area fraction of the matrix was observed, with a concomitant reduction in the bright BSE-contrast phase. After subsequent aging at 900 °C similar area fractions were observed between the cast-aged and SHT-A samples. For the higher temperature exposures, the SHT-A samples displayed broadly similar behavior. The most notable differences between these results and the higher temperature cast-aged results were the lower matrix fractions coupled with the higher dark BSE-contrast

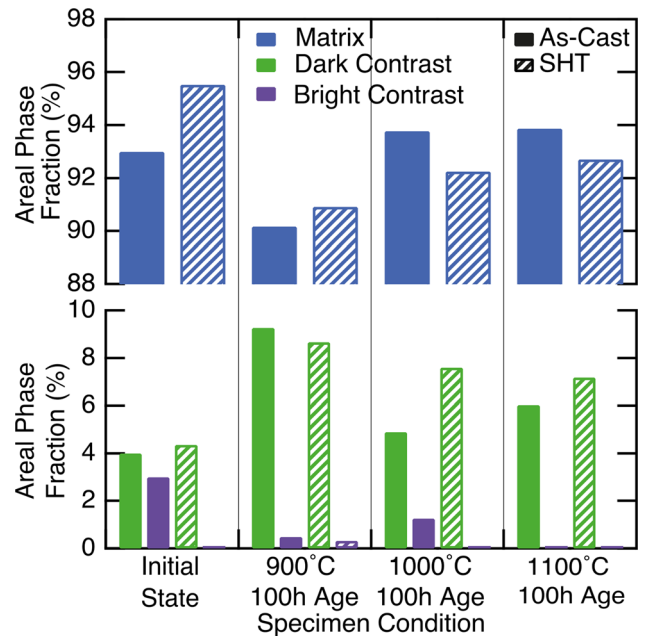


Fig. 4—Phase fractions of the as-cast, as-cast-aged specimens (solid bars) and the SHT, SHT-A specimens (striped bars) (Color figure online).



fractions in the SHT-A samples and the absence of the bright BSE-contrast phase in the SHT-A 1000 °C sample.

### B. Carbide Evolution in Heat-Treated Co-101

The high-temperature phase transformations of Co-101 aged for 1, 10, and 100 hours are shown in the DSC thermograms of Figures 5(a) through (c), respectively. All specimens contained an endothermic peak at approximately 1360 °C to 1370 °C corresponding to bulk melting of the alloy, and a second endothermic peak at approximately 1290 °C relating to the melting of one of the interdendritic phases. Additionally, a third endothermic peak was also observed at 1230 °C for some of the specimens. This peak was observed to disappear in the specimens that had been exposed to temperatures greater than 1250 °C for 1 hour, 1150 °C for 10 hours, and 1100 °C for 100 hours, highlighted by the red traces in Figure 5. The loss of this peak coincided with the reduction of the bright BSE-contrast  $M_{23}C_6$  phase in the contour maps of areal phase fraction. This suggests the peak corresponded to the dissolution temperature of this interdendritic phase. With the formation of the dark BSE-contrast precipitates observed in the heat-treated Co-101 alloys, it may be anticipated that an additional peak would be observed in the DSC thermograms of these specimens. However, no such peak could be identified in the thermogram. The lack of an additional peak could imply that the dissolution temperature of the precipitates was strongly

obscured by the large interdendritic melting event at 1290 °C.

Previous electron diffraction studies have identified the phases in as-cast Co-101 as the face-centered cubic  $\gamma$  matrix, the Cr-rich  $M_7C_3$ , and the Cr- and Mo-rich  $M_{23}C_6$  carbide, with the former carbide possessing a dark BSE contrast, and the latter a bright BSE contrast.<sup>[12]</sup> As observed in the SEM micrographs and the DSC thermograms, exposing Co-101 to different temperatures modifies the carbide constituents in the alloy, including the dissolution of the bright contrast  $M_{23}C_6$  carbide. The variation in contrast across the dark  $M_7C_3$  carbide after certain heat treatments suggests an additional transformation of the interdendritic carbides. While the DSC thermograms include evidence for the loss of the  $M_{23}C_6$  carbide, no features were observed in the thermogram that were consistent with transformation of the  $M_7C_3$  interdendritic carbide. Insights into the nature of the carbides formed during solidification and their subsequent transformation during thermal exposure were sought through thermodynamic calculations using the Thermo-Calc software.

Plots of the phase fractions as a function of temperature predicted using the Thermo-Calc software assuming equilibrium and Scheil solidification conditions are shown in Figure 6(a). The calculations suggest that the liquidus temperature is 1342 °C, lower than that observed experimentally in the DSC data. Under both solidification assumptions, the first carbide predicted to form is  $M_7C_3$ , which commences around 1240 °C. This is consistent with the large endothermic event seen in the

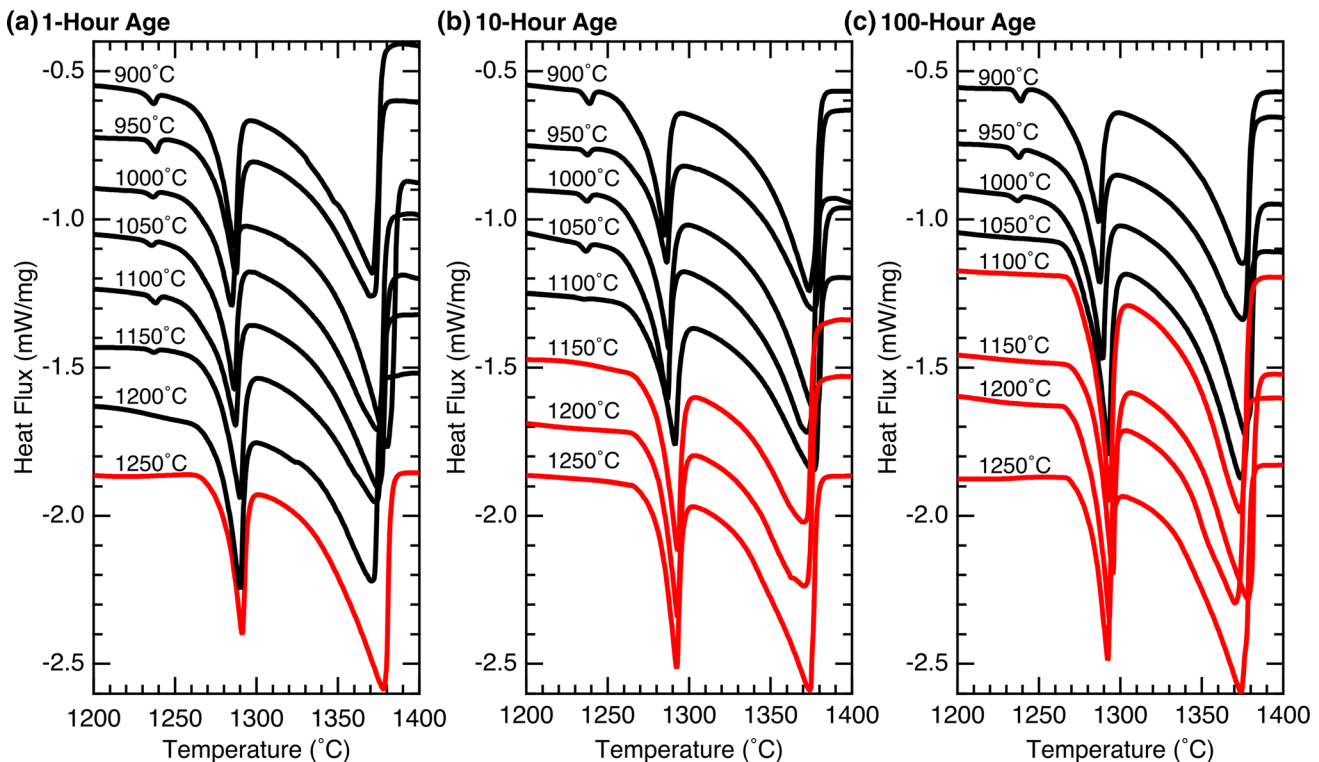


Fig. 5—DSC thermograms on heating of post-heat-treated Co-101 specimens exposed at their corresponding temperature for 1, 10, and 100 h, (a to c), respectively. The red curves identify the thermograms containing only two endothermic peaks (Color figure online).

DSC data. Under equilibrium conditions, solidification is predicted to terminate around 1224 °C, again in broad agreement with the DSC data. Only below 1116 °C is  $M_{23}C_6$  predicted to become stable. In contrast, Scheil solidification conditions predict that  $M_7C_3$  carbides will continue to form down to 1180 °C, below which the formation of  $M_7C_3$  ceases in favor of  $M_{23}C_6$ . At lower temperatures and higher volume fractions of solid, the Scheil simulation predicts the formation of a Mo-rich silicide phase. While Mo-rich phases are observed in the as-cast microstructure, no evidence of such phases was detected, suggesting the alloy does not fully follow Scheil solidification behavior to high volume fractions of solid.

The XRD patterns of the 950 °C, 1000 °C, 1050 °C, and 1100 °C Co-101 specimens, heat treated for 1, 10, and 100 hours are shown in Figure 7. The diffraction peak intensities varied non-systematically, consistent with appreciable texture arising as a result of the casting process. All diffraction patterns contained a peak at 47 deg  $2\theta$ , indicative of the martensitic transformation of the  $\gamma$  phase into the hexagonal  $\epsilon$  phase at high temperatures or during quenching. Despite the high intensity of the  $\gamma$  and  $\epsilon$  peaks, the minor phase peaks could still be observed. The overlap between the minor phase peaks and the strong  $\gamma$  phase made analysis of the minority phases challenging, particularly in samples with strong crystallographic texture. Nevertheless,

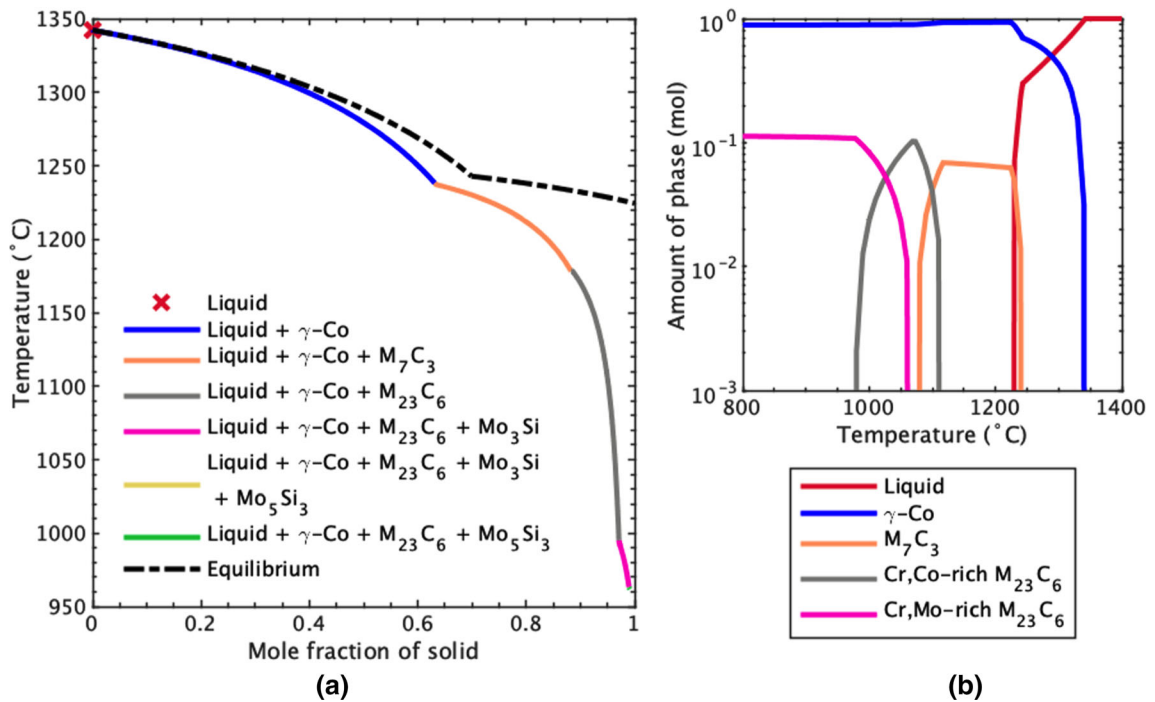


Fig. 6—Thermo-Calc predictions using the SSOL5 database of the fraction solid as a function of temperature for Co-101 assuming either equilibrium (dashed line) or Scheil (colored line) solidification conditions (a). The colors indicate the phases present in the Scheil solidification. Thermo-Calc predicted equilibrium phases between 800 °C and 1400 °C (b) (Color figure online).

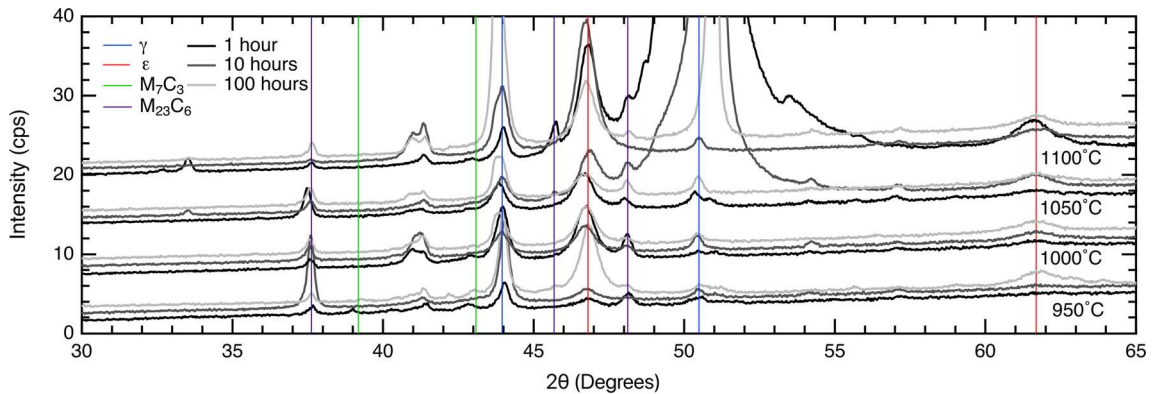


Fig. 7—XRD patterns of 950 °C to 1100 °C cast-aged Co-101 specimens with the characteristic peaks of each phase highlighted.



characteristic peaks, as identified by a full pattern Pawley refinement, for the  $M_7C_3$  were located at 39 and 43 deg  $2\theta$  and peaks for the  $M_{23}C_6$  were located at 37.5, 46, and 48 deg  $2\theta$ . The characteristic peaks for  $M_7C_3$  were observed in the XRD data obtained from all specimens except those that had been subjected to times and temperatures exceeding: 100 hours at 1000 °C, 10 hours at 1050 °C, or 1 hour at 1100 °C. The  $M_{23}C_6$  carbide peaks were observed in all diffraction patterns due to the presence of the primary interdendritic  $M_{23}C_6$ , the formation of  $M_{23}C_6$  as a transformation product of the  $M_7C_3$  interdendritic phase, or due to the precipitation of the  $M_{23}C_6$  within the  $\gamma$  matrix phase. The peaks present in the XRD data around 41 deg  $2\theta$  could not be unambiguously assigned as both the  $M_{23}C_6$  and  $M_7C_3$  have peaks in this range. While the characteristic peaks of the minor phases were occasionally obscured by the dominant  $\gamma$  or  $\epsilon$  peaks in the diffraction patterns from some of the specimens, cross-checking with the SEM micrographs for contrast variations across the interdendritic phase was used as a means of identification of the  $M_7C_3$  to  $M_{23}C_6$  transformation.

### C. Precipitation and Hardness Behavior of Heat-Treated Co-101

A key microstructural feature of the heat-treated Co-101 alloys was the secondary precipitates that form within the  $\gamma$  matrix. The PSDs of the precipitates in the heat-treated Co-101 specimens after 1, 10, and 100 hours of aging are displayed as box-whisker plots in Figures 8(a) through (c), respectively. The box widths represent the 25th and 75th percentiles, the whiskers represent the 10th and 90th percentiles, and the red markers represent the mean values of the distributions. The total number of precipitates per 0.039 mm<sup>2</sup> of each specimen are summarized in Figure 8(d). A plot of the areal phase fraction as a function of aging temperature derived from these results is available in the Supplementary Information. However, the statistical variations in precipitate density across the microstructure resulted in relatively large uncertainties in these areal fraction data.

After 1 hour of aging, Figure 8(a), the mean precipitate size with respect to temperature exhibited a C-shaped relationship, with the 900 °C and 1250 °C specimens possessing the smallest precipitate mean sizes and the 950 °C to 1200 °C specimens possessing similar mean values. The 900 °C specimen showed a narrower PSD, suggesting a relatively higher precipitate nucleation rate compared to the growth rate. In contrast, in the 1250 °C specimen, the rate of dissolution of the precipitates was as great as nucleation, preventing the precipitate embryos from growing to larger sizes. Consequently, the 900 °C specimen contained many precipitates, whereas the 1250 °C specimen contained almost no precipitates, as shown in Figure 8(d). For the 950 °C to 1200 °C specimens, the temperature enabled accelerated growth of the precipitate embryos, attaining a larger average size and wider PSDs compared to the 900 °C specimen. Although the PSDs obtained after exposure at all the

temperatures considered were visually similar, the total number density of precipitates peaked in the 1000 °C specimen and decreased with further increases in temperature.

After 10 hours of aging, Figure 8(b), the C-shaped relationship between the mean precipitate size and temperature in the 1-hour condition was not observed. With this exposure duration, the mean size of the PSD was consistent between the 900 °C and 1100 °C specimens, with only the 1150 °C and 1200 °C specimens exhibiting an appreciable increase in mean size. No precipitates were present in the 1250 °C specimen, as observed in the micrograph of Figure 3(a). The PSD widths decreased following exposure at increasing temperature from 900 °C to 1000 °C. The number density of precipitates in the specimens followed a similar trend to the 1-hour specimens, peaking in number within the 1000 °C specimen and decreasing following exposure at higher temperatures.

After 100 hours of aging, Figure 8(c), the mean precipitate sizes of the specimens were typically similar to the respective 10-hour temperature exposures except for the 1100 °C specimen, which exhibited a significantly larger mean precipitate size. At this exposure time, no precipitates were observed at 1200 °C or 1250 °C. The PSD widths were similar to those observed after 10 hours at the same temperatures. The exception to this observation was the 1000 °C specimen, which possessed a significantly wider PSD compared to its 10-hour counterpart. However, the PSD widths were significantly broader for the 1000 °C and 1100 °C specimens. As previously observed, the number density of precipitates peaked in the 1000 °C specimen and decreased in samples exposed at higher temperatures.

Along with other microstructural changes, the effects of precipitation were likely to modify the hardness of the Co-101 alloy. Co-101, in its as-cast state, possessed a hardness of 318 HV. The changes to the hardness after applying different heat treatment conditions are displayed as a contour map in Figure 9. The hardness behavior could be separated into three distinct temperature ranges: 900 °C to 950 °C, 950 °C to 1100 °C, and 1100 °C to 1250 °C. In the 900 °C to 950 °C temperature range, the hardness increased from approximately 330 HV after 1 hour to approximately 350 HV after 10 hours, with the hardness remaining consistent thereafter. Maximum hardness of the cast-aged alloys was achieved within the 1000 °C to 1050 °C temperature range. Hardness values of 380 HV were attained after 10 and 1 hours of exposure at 1000 °C and 1050 °C, respectively. Exposures for longer durations at these temperatures softened Co-101 to 350-370 HV. The final temperature range, 1100 °C to 1250 °C, exhibited no peak in hardness, with the hardness tending to increase slightly with aging time at all temperatures within this range. Furthermore, within this temperature range, the greater the exposure temperature, the softer the alloy tended to be.

The effects of an SHT followed by a 100-hour age on the PSD of the precipitates are demonstrated in Figure 10(a). Increasing the aging temperature results

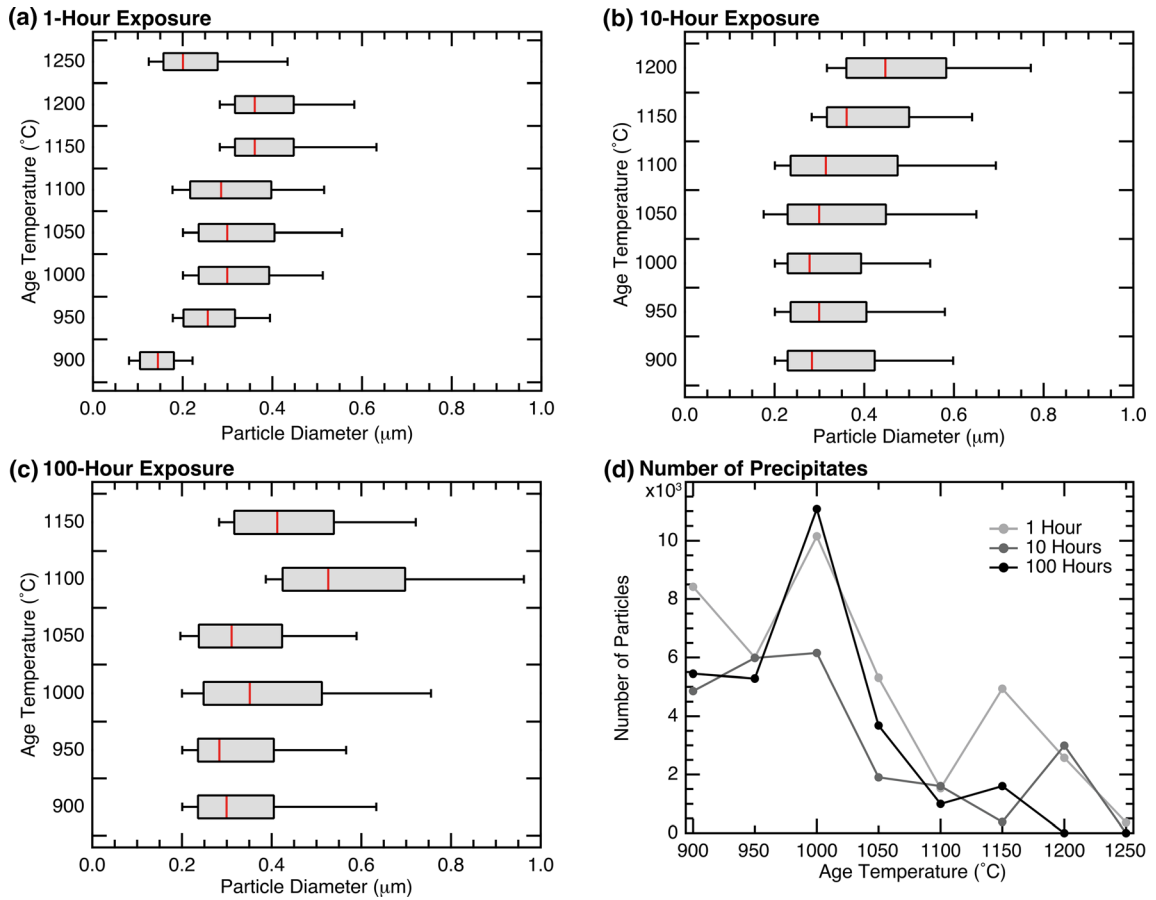


Fig. 8—PSDs of the precipitates in cast Co-101 after aging at different temperatures for 1, 10, and 100 h, (a to c) respectively, and the total number of precipitates per 0.039 mm<sup>2</sup> area of each specimen, (d).

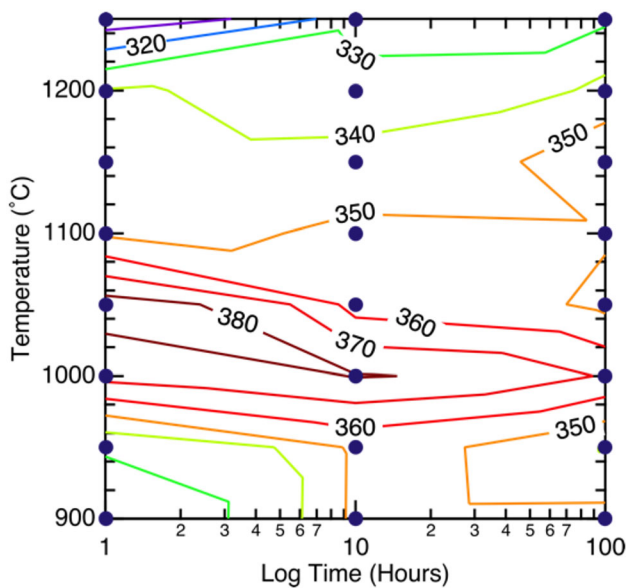


Fig. 9—Contour plot of Vickers hardness of cast and aged Co-101 as a function of time and temperature (Color figure online).

in an increase in the mean size and PSD widths. Furthermore, the number density of precipitates in the specimens decreased with increasing aging

temperature. Compared to the cast-aged 100-hour specimens, the corresponding SHT-A specimens possessed significantly smaller average precipitate sizes and PSD widths. This suggests that the SHT increases the homogeneity of the precipitates that form during the age, compared to the cast-aged Co-101 alloys. However, it should be noted that the number density of precipitates that formed in the SHT-A specimens was also modified. The SHT-A 900 °C specimen contained more than three times as many precipitates as the 900 °C 100-hour cast-aged specimen. The SHT-A 1000 °C specimen possessed fewer than half of that of the 1000 °C 100-hour cast-aged specimen, while the SHT-A 1100 °C specimen had more than twice as many precipitates as the 1100 °C 100-hour cast-aged specimen.

Comparisons between the hardness of the as-cast, cast-aged, SHT, and SHT-A specimens are shown in Figure 10(b). The hardness of the SHT and SHT-A 900 °C specimens were found to be superior to that of the as-cast and cast-aged 900 °C 100-hour specimens. The SHT-A 900 °C specimen possessed one of the highest hardness values of any heat-treated Co-101 samples. However, the SHT-A 1000 and 1100 °C specimens were significantly softer than their cast-aged counterparts. The SHT-A 1100 °C specimen exhibited a hardness similar to that of the as-cast state.

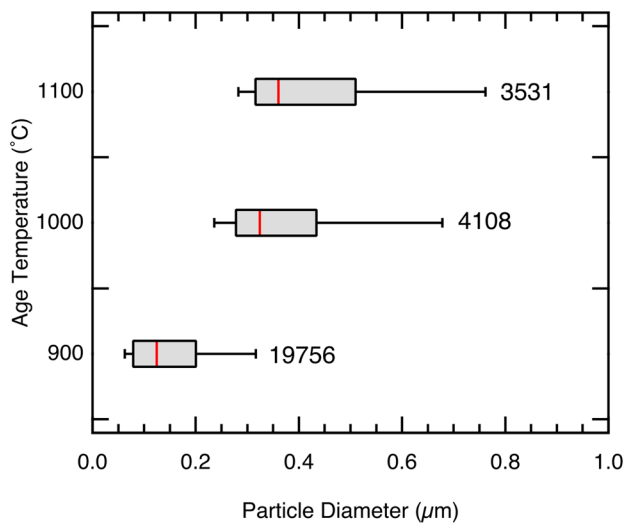
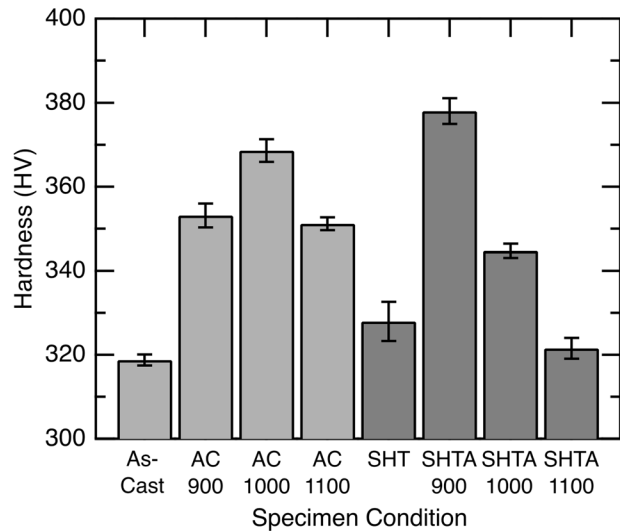
**(a) SHTA PSDs****(b) SHTA and Cast-Aged Hardness**

Fig. 10—(a) PSDs of the precipitates in the SHT-A specimens. The number of precipitates per 0.039 mm<sup>2</sup> specimen area for each PSD is shown adjacent to each distribution. (b) Comparison of the Vickers hardness values between the as-cast (AC), 100-h cast-aged, the SHT, and SHT-A Co-101 alloys.

## IV. DISCUSSION

### A. Carbide Transformations and the Effects on Precipitation

The effects of heat treatment on the microstructure of Co-101 are complex, especially those relating to the carbide constituents. In the as-cast state, Mo-rich  $M_{23}C_6$  was observed, the occurrence of which cannot be rationalized by assuming equilibrium conditions as solidification is predicted to terminate with  $M_7C_3$ . However, Mo is predicted to preferentially partition to the liquid during solidification. As such, under Scheil solidification conditions, the  $M_{23}C_6$  can be formed during solidification below 1180 °C as a result of solidification-induced microsegregation to the interdendritic regions. This  $M_{23}C_6$  is predicted to contain excess Mo. For example, the composition of  $M_{23}C_6$  at 95 pct solid (at approximately 1100 °C) is predicted to be 69.3Cr-20.7C-9.1Mo-0.9Fe-0.03Ni (mol pct). In comparison, the equilibrium composition of  $M_{23}C_6$  at 1100 °C is comparatively lean in Mo, being 69.1Cr-20.7C-0.02Mo-0.07Fe-0.1Ni (mol pct). In addition,  $M_{23}C_6$  with appreciable solubility for Mo is only predicted below approximately 1069 °C under equilibrium conditions (Figure 6(b)). These predictions therefore support the observation of a non-equilibrium Mo-rich  $M_{23}C_6$  carbide in the as-cast microstructure, arising as a result of solidification-induced microsegregation.

During high-temperature heat treatments, the partial dissolution of the primary  $M_{23}C_6$  interdendritic carbide and the redistribution of Mo enrich the matrix phase with additional C, Cr, and Mo. The flux of these precipitate-forming elements may be expected to produce a concentration gradient between the interdendritic regions and dendrite cores. Therefore, the peripheries of the dendrites are the first regions to achieve the

concentration of elements necessary for precipitation. Over longer durations of exposure, sufficient diffusion occurs for precipitation to be induced deeper within the dendrites. These effects are evident from the varying precipitate sizes and number densities between these regions. This may also be expected to lead to an increase in the width of the precipitate size distribution as particles nucleating near the interdendritic primary carbides grow, and nucleation of new carbides subsequently occurs deeper within the grains. For the samples heat treated at 900 °C to 1000 °C, the occurrence of a bright contrast phase may be rationalized by the increase in predicted Mo solubility in the  $M_{23}C_6$  carbide below 1069 °C from the equilibrium Thermo-Calc simulations.

At elevated temperatures below the  $M_{23}C_6$  solvus (~1116 °C), the transformation of the interdendritic  $M_7C_3$  into the  $M_{23}C_6$  carbide should also be considered with regard to its influence on precipitation. This carbide transformation liberates additional C and Cr, which would be expected to further contribute to the flux of precipitate-forming elements into the dendrites. This behavior was similarly reported by Gui *et al.*<sup>[17]</sup> where the release of carbide-forming elements into the  $\gamma$  matrix was observed *in-situ* during the transformation of the primary  $M_7C_3$  into the  $M_{23}C_6$  carbide at temperatures exceeding 1140 °C. This, along with the greater diffusion rates in Co-101 expected at higher temperatures, explains why a larger number of precipitates were observed deeper into the dendrites in the 1000 °C to 1050 °C specimens compared to the 900 °C to 950 °C specimens.

In the specimens exposed to temperatures exceeding 1100 °C, the rate of dissolution of the precipitates was significantly greater. Compared to the lower temperature conditions, these specimens contained substantially fewer precipitates within their microstructures. The



precipitates were predominantly located at the periphery of the dendrites, similar to the specimens exposed at 900 °C to 950 °C. However, these precipitates were larger than those observed in the 900 °C to 950 °C specimens, with wider PSDs that were skewed to larger sizes.

With the lack of precipitates, the complete dissolution of the primary  $M_{23}C_6$  carbide, and the fully transformed  $M_{23}C_6$  interdendritic carbide network, the 1250 °C 10-hour condition was considered an appropriate condition for SHT. As significant carbon was taken into solution during the SHT, the subsequent aging induced precipitation without the requirement of long-distance diffusion between the interdendritic regions and dendrite cores. All the precipitate embryos that formed during the SHT-A would have likely formed within a short period and, therefore, all experienced a similar growth time. Consequently, the precipitates that formed were smaller and more equally distributed throughout the dendrites compared to the cast-aged specimens. This explains why narrower PSDs were observed in all the SHT-A specimens.

### B. Rationalizing the Contribution of the Intragranular Carbides to the Hardness of Co-101

The influence of the transformation of the interdendritic carbide network on the mechanical properties was previously studied by Gui *et al.*<sup>[13]</sup> In their study, it was found that Co-based superalloys possessing an  $M_{23}C_6$  interdendritic network had superior stress-rupture life compared to those with an  $M_7C_3$  interdendritic carbide network or secondary precipitation of  $M_{23}C_6$ . This behavior was attributed to the increased stability of the coherent cubic–cubic  $M_{23}C_6$ - $\gamma$  interface compared to the incoherent hexagonal–cubic  $M_7C_3$ - $\gamma$  interface. The coherent interface between  $M_{23}C_6$  and  $\gamma$  increased resistance to decohesion between the phases during deformation. The precipitation from the cast-aged specimen was found to overage rapidly during the mechanical test, leading to a decrease in stress-rupture life. Due to the similarity of the carbide transformations occurring in Co-101, with  $M_7C_3$  transforming to  $M_{23}C_6$  and an increase in intragranular  $M_{23}C_6$ , it is possible that heat-treated Co-101 may exhibit similar benefits in creep behavior.

Precipitation is known to affect the hardness of an alloy by impeding dislocation motion, which is governed by the balance between the Friedel Effect<sup>[18]</sup> of precipitate shearing, and the stress required for dislocations to bypass obstructions by Orowan Bowing.<sup>[19]</sup> Optimal hardening for a given volume fraction is achieved with the precipitate separation that corresponds to the transition between these two mechanisms. In this regard, the PSDs of the heat-treated alloys provide insights into the measured hardness behavior of the Co-101 specimens. Maximum hardness of the cast-aged specimens was achieved in the 1000 °C 10-hour age and 1050 °C 1-hour age. Interestingly, the PSDs of Co-101 after both these heat treatments contained similar mean average sizes, distribution widths, and total number of

precipitates per unit area. The cast-aged specimens that deviated from these PSD characteristics were softer, which may be attributed to either the precipitates being smaller, and therefore easier to shear, or by being larger and increasing the precipitate separation, reducing the stress required for Orowan Bowing.

In the SHT-A specimens, the homogeneity of the precipitate dispersions may have assisted in reducing the average separation between precipitates. Indeed, the SHT-A 900 °C specimen possessed one of the highest hardness values of all the heat-treated Co-101 alloys. Despite the greater number of precipitates, compared to the cast-aged specimens, the sizes of the precipitates were significantly smaller than the 1000 °C 10-hour and 1050 °C 1-hour specimens. The smaller precipitate size reduced the stress required for shearing, but the large number of precipitates reduced the distance separating them, thereby increasing the Orowan stress. Importantly, it should be noted that the hardness of the 1000 °C and 1050 °C cast-aged specimens peaked much earlier during exposure. The SHT-A 900 °C specimen achieved its hardness after 100 hours of exposure, suggesting that high hardness values could be obtained after longer exposure durations. The narrower distribution of the precipitate sizes also increases the precipitate size stability, by reducing the effects of Ostwald ripening. Furthermore, this specimen may achieve even greater values of hardness past 100 hours of aging, whereas the 1000 °C and 1050 °C cast-aged specimens would be expected to soften further. Critically, the SHT also allows the elemental constituents of the carbides to be more homogeneously distributed throughout the matrix phase. In a study of the effect of heat treatment on a directionally solidified Co-based alloy based on X-40 by Jiang *et al.*,<sup>[20]</sup> heat treatment for 24 h between 750 °C and 950 °C improved the 0.2 pct yield stress, the ultimate tensile strength, and the stress-rupture life at 980 °C, but these improvements were all achieved at the expense of ductility. Similar benefits may be expected from heat treatment of Co-101, although further studies are required to ascertain which properties are improved and which are compromised.

## V. CONCLUSIONS

The microstructure and hardness of the Co-based superalloy Co-101 have been studied after a range of heat treatments to assess the benefits that may be derived from solution heat treatment and aging or by aging directly from the as-cast state. From these studies, the following conclusions could be drawn:

- Aging of the cast-aged specimens resulted in dissolution of the interdendritic  $M_{23}C_6$  carbide, transformation of the interdendritic  $M_7C_3$  into the  $M_{23}C_6$  carbide, and the precipitation of a carbide phase within the matrix.
- Aging at lower temperatures favored precipitation over the transformation of the interdendritic constituents, at intermediate temperatures the

transformation of interdendritic phases enhanced precipitation, and at high-temperature transformation of the interdendritic constituents was accelerated with precipitation being suppressed.

- Individual cast-aged specimens exhibited a wide range of precipitate sizes, which were likely a result of diffusion between the interdendritic regions and the matrix. These precipitates were susceptible to coarsening and agglomeration over longer exposure times due to Ostwald ripening.
- The solution heat-treated and aged specimens possessed interdendritic carbide networks dominated by  $M_{23}C_6$  accompanied by  $M_{23}C_6$  precipitation within the matrix phase.
- The intragranular carbides were found to be generally greater in number, more homogeneously distributed, and more consistent in size to each other in the solution heat-treated and aged states. These features were believed to give rise to the improved hardness observed for the Co-101 alloy in the solution-aged state.

### ACKNOWLEDGMENTS

The authors gratefully acknowledge the assistance of Dr H.T. Pang and S. Rhodes in performing the experiments. For the purpose of open access, the author has applied a Creative Commons Attribution (CC BY) licence to any Author Accepted Manuscript version arising from this submission.

### FUNDING

Funding to support this work is acknowledged from Knauf Insulation Ltd.

### CONFLICT OF INTEREST

The authors declare the following financial interests/personal relationships which may be considered as potential competing interests: James Moffat reports financial support was provided by Knauf Insulation Ltd.

### RESEARCH DATA

The underlying research data required to reproduce these findings are available from the University of Cambridge repository.

### OPEN ACCESS

This article is licensed under a Creative Commons Attribution 4.0 International License, which permits use, sharing, adaptation, distribution and reproduction in any medium or format, as long as you give appropriate credit to the original author(s) and the source,

provide a link to the Creative Commons licence, and indicate if changes were made. The images or other third party material in this article are included in the article's Creative Commons licence, unless indicated otherwise in a credit line to the material. If material is not included in the article's Creative Commons licence and your intended use is not permitted by statutory regulation or exceeds the permitted use, you will need to obtain permission directly from the copyright holder. To view a copy of this licence, visit <http://creativecommons.org/licenses/by/4.0/>.

### SUPPLEMENTARY INFORMATION

The online version contains supplementary material available at <https://doi.org/10.1007/s11661-023-07283-7>.

### REFERENCES

1. D.L. Klarstrom: *J. Mater. Eng. Perform.*, 1993, vol. 2, pp. 523–30.
2. M. Riddihough: *Tribology*, 1970, vol. 3, pp. 211–15.
3. C.P. Sullivan, M.J. Donachie, F.R. Morral: *Cobalt-base superalloys*, Centre d'Information du Cobalt, 1970.
4. C.T. Sims: *JOM*, 1969, vol. 21, pp. 27–42.
5. C.P. Sullivan, J.D. Varin, and M.J. Donachie Jr.: *Met. Eng. Q.*, 1969, vol. 9, pp. 16–29.
6. R. Ahmed, H.V. de Lovelock, N.H. Faisal, and S. Davies: *Tribol. Int.*, 2014, vol. 80, pp. 98–114.
7. A.L. Ramirez, J. Porcayo-Calderon, Z. Mazur, V.M. Salinas-Bravo, L. Martinez-Gomez: *Adv. Mater. Sci. Eng.*, 2016, Article ID 1745839.
8. S. Zangeneh and H. Farhangi: *Mater. Des.*, 2010, vol. 31, pp. 3504–11.
9. S. Zangeneh, H.R. Lashgari, and M. Asnavandi: *Eng. Failure Anal.*, 2018, vol. 84, pp. 276–86.
10. W.H. Jiang, H.R. Guan, and Z.Q. Hu: *Mater. Sci. Eng. A*, 1999, vol. 271, pp. 101–08.
11. D.L. Klarstrom: Heat Treatment of Cobalt-Base Alloys, *ASM Handbook*, Vol. 4E, G.E. Totten & D.S. MacKenzie (eds), 2016.
12. J.P. Moffat, T.E. Whitfield, K.A. Christofidou, E.J. Pickering, N.G. Jones, and H.J. Stone: *Metals*, 2020, vol. 10, p. 248.
13. W. Gui, H. Zhang, M. Yang, T. Jin, X. Sun, and Q. Zheng: *J. Alloys Compd.*, 2017, vol. 728, pp. 145–51.
14. M. Wang, D. Flahaut, Z. Zhang, and I.P. Jones: *J. Alloys Compd.*, 2019, vol. 781, pp. 751–60.
15. K. Wiczerzak, P. Bala, R. Dziurka, T. Tokarski, G. Cios, T. Koziel, and L. Gondek: *J. Alloys Compd.*, 2017, vol. 698, pp. 673–84.
16. C.A. Schneider, W.S. Rasband, and K.W. Eliceiri: *Nat. Methods*, 2012, vol. 9, pp. 671–75.
17. W. Gui, H. Zhang, M. Yang, T. Jin, X. Sun, and Q. Zheng: *J. Alloys Compd.*, 2017, vol. 695, pp. 1271–78.
18. J. Friedel: *Dislocations*, Pergamon Press, London, 1964.
19. E. Orowan: *Symposium on Internal Stresses in Metals and Alloys*, Institute of Metals; Faraday Society pp. 447, 1948.
20. W.H. Jiang, H.R. Guan, and Z.Q. Hu: *Metall. Mater. Trans. A*, 1999, vol. 30A, pp. 2251–54.

**Publisher's Note** Springer Nature remains neutral with regard to jurisdictional claims in published maps and institutional affiliations.